INTERNATIONAL JOURNAL FOR NUMERICAL METHODS IN ENGINEERING
Int. J. Numer. Meth. Engng 2006; **65**:2221–2245
Published online 26 October 2005 in Wiley InterScience (www.interscience.wiley.com). DOI: 10.1002/nme.1535

Crush dynamics of square honeycomb sandwich cores

Zhenyu Xue and John W. Hutchinson*, †

Division of Engineering and Applied Sciences, Harvard University, Cambridge, MA 02138, U.S.A.

SUMMARY

Square honeycombs are effective as cores for all-metal sandwich plates in that they combine excellent crushing strength and energy absorption with good stiffness and strength in out-of-plane shear and in-plane stretch. In applications where sandwich plates must absorb significant energy in crushing under intense impulsive loads, dynamic effects play a significant role in the behaviour of the core. Three distinct dynamic effects can be identified: (i) inertial resistance, (ii) inertial stabilization of webs against buckling, and (iii) material strain-rate dependence. Each contributes to dynamic strengthening of the core. These effects are illustrated and quantified with the aid of detailed numerical calculations for rates of deformation characteristic of shock loads in air and water. A continuum model for high rate deformation of square honeycomb cores is introduced that can be used to simulate core behaviour in large structural calculations when it is not feasible to mesh the detailed core geometry. The performance of the continuum model is demonstrated for crushing deformations. Copyright © 2005 John Wiley & Sons, Ltd.

KEY WORDS: honeycomb cores; sandwich plates; dynamic loads; material rate dependence; dynamic buckling; plastic buckling

1. INTRODUCTION

All-metal sandwich plates have distinct advantages over monolithic plates of equal mass in applications to structures designed to withstand intense short-duration pressure pulses, especially in water environments [1, 2]. To be effective under intense impulsive loads, a sandwich plate must be able to dissipate in core crushing a significant fraction of the kinetic energy initially acquired [1, 2]. Consequently, if a plate is to retain its integrity with only limited crushing, its core must have ample crushing strength and energy-absorbing capacity. Square honeycomb cores have been shown to be one of the best choices from this point of view. In addition, they

*Correspondence to: John W. Hutchinson, Division of Engineering and Applied Sciences, Harvard University, Pierce Hall, 29 Oxford Street, Cambridge, MA 02138, U.S.A.
†E-mail: hutchinson@husm.harvard.edu

Contract/grant sponsor: ONR; contract/grant numbers: N00014-02-1-0700, GG10376-114934
Contract/grant sponsor: Harvard University

Received 31 January 2005
Revised 20 June 2005
Accepted 17 August 2005

have in-plane strength that contributes to dissipation in overall stretching of the plate and they provide good transverse shear strength.

Strong dynamic effects come into play in the behaviour of the core when sandwich plates are subject to intense pressure pulses. An important dimensionless parameter governing inertial effects is $V_0/(c_0\varepsilon_Y)$, where V_0 is the relative velocity of the sandwich faces, $c_0=\sqrt{E/\rho}$ is the elastic wave speed of the web material, and E, ρ and ε_Y are the Young's modulus, density and initial yield strain of the metal [3]. To motivate the study in this paper, consider a full-scale plate with core thickness, $H=0.1\,\mathrm{m}$, whose front face towards the shock is set in motion with velocity in the range $20\,\mathrm{m\,s^{-1}}<V_0<200\,\mathrm{m\,s^{-1}}$, where the upper limit of this range is representative for strong water shocks. The time scale of the pressure pulse is often sufficiently short such that the back face and much of the core remain nearly motionless while the front face acquires its initial velocity. Much of core crushing takes place in the period after the front face has been set in motion and before the back face accelerates to the same velocity as the front face. The associated average strain-rate range in the core is $200\,\mathrm{s^{-1}}<\dot{\bar{\varepsilon}}<2000\,\mathrm{s^{-1}}$. Material strain-rate dependence is clearly important. Two other dynamic effects also significantly affect core behaviour even more than material rate dependence in the range of relative velocities relevant here that satisfy $V_0/(c_0\varepsilon_Y)>5$. The most obvious is simply the inertial resistance of the core to the motion of the front face sheet and the consequent plastic wave propagation induced in the core webs. Less obvious is the inertial stabilization of the webs that delays the onset of web buckling thereby maintaining the effective strength of the core to much larger crushing strains than under quasi-static crushing. Web stabilization also significantly increases the energy-absorbing capacity of the webs. These two inertial effects combine together in a complex way.

Considerable effort has addressed the crushing behaviour of hexagonal honeycombs for applications where energy absorption is important [4–6]. Most of these studies differ from the present one in several respects. The honeycomb thickness to hexagonal cell size is usually large, while the sandwich plates of interest here have a core thickness to cell size typically on the order of unity (Figure 1). More importantly, the relative velocity imposed on the honeycomb is usually lower (e.g. $V_0/(c_0\varepsilon_Y)<5$) and not sufficient to activate the strong inertial effects that occur under blast loads. Relatively few studies of dynamic plastic crushing have addressed problems in the range of interest here ($V_0/(c_0\varepsilon_Y)>5$), where plastic wave propagation and plastic buckling are tightly coupled. The speed at which a plastic wave front propagates along a straight bar or web can be expressed in terms of quantities behind the front according to

$$c_P=\mathrm{e}^{-\varepsilon}\sqrt{(E_t-\sigma)/\rho}\cong\sqrt{E_t/\rho} \tag{1}$$

where σ and ε are the true stress and strain and E_t is the tangent modulus of the true stress–strain curve [3, 7, 8]. For convenience, the small strain expression approximation, $c_P=\sqrt{E_t/\rho}$, is used for discussion purposes in this paper.

The roles of inertial and material strain-rate in energy absorption under dynamic compression have been elucidated in Reference [9] for two distinct types of structures: those that undergo relatively gradual buckling such as columns and those that tend to be more imperfection-sensitive and catastrophic such as shells. The structural members of interest here fall into the first category, but the loading rates discussed in Reference [9] are considerably slower than will be considered here. To gain further appreciation of the time scales involved in the problems of interest here, consider a flat steel core web of a sandwich plate having a core

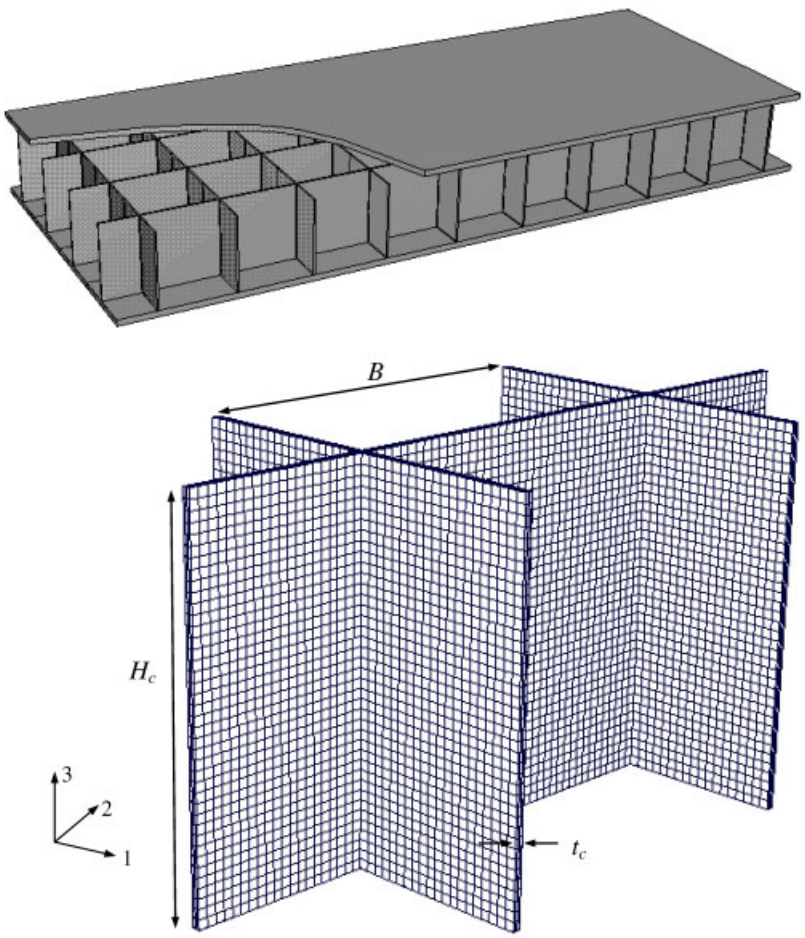

Figure 1. Sandwich plate with a square honeycomb core and unit cell used for computing the crushing behaviour of the square honeycomb core with representative finite-element mesh.

thickness $H = 0.1\,\mathrm{m}$ whose front face abruptly accelerated to a velocity $V_0 = 100\,\mathrm{m\,s^{-1}}$ and whose back face is held fixed (loading #2 in Figure 2). For typical elastic and plastic wave speeds, $c_0 = 5000\,\mathrm{m\,s^{-1}}$ and $c_P = 500\,\mathrm{m\,s^{-1}}$, the elastic and plastic wave fronts reach the back face at times $t = 0.2 \times 10^{-4}\,\mathrm{s}$ and $0.2 \times 10^{-3}\,\mathrm{s}$, respectively. Note that by the time the plastic wave reaches the back face, the overall strain experienced by the core is relatively large: $\bar{\varepsilon} \equiv V_0 t/H = 0.2$. It will be seen later that these estimates are realistic. Inertia can stabilize the webs such that they remain unbuckled before the plastic wave front reaches the back face with the results that the webs exert much greater force on the front face and absorb more energy than they would under quasi-static loading. For this example, $V_0/(c_0\varepsilon_Y) = 10$ (assuming $\varepsilon_Y = 0.002$) and the overall strain-rate is $\dot{\bar{\varepsilon}} = V_0/H = 10^3\,\mathrm{s^{-1}}$. The feature that distinguishes crushing in the range of applied velocities of interest here is the fact that substantial core

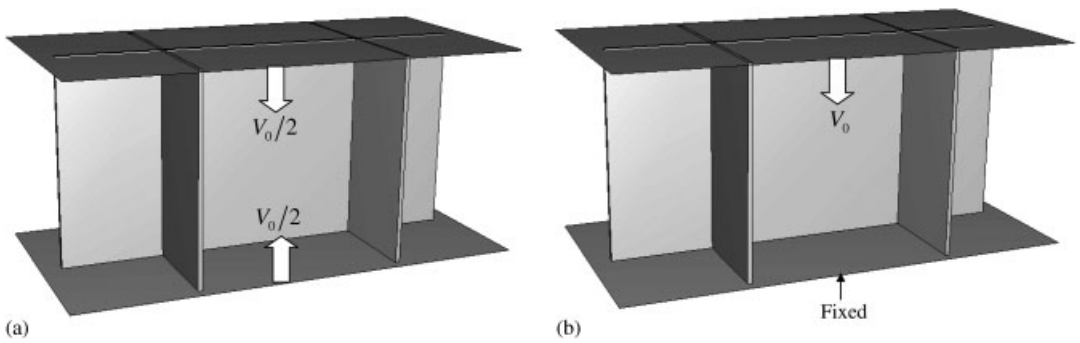

Figure 2. Two compressive constant crushing-rate loadings on unit cell of square honeycomb: (a) loading #1; and (b) loading #2.

straining occurs during the period while the plastic wave is propagating through the core web and prior to web buckling.

In addition to detailing the dynamic phenomena noted above, a continuum model for multi-axial stressing of metallic sandwich cores will be proposed that is capable of approximately replicating the three aspects of dynamic core behaviour just cited. The continuum model is intended for use in finite-element analyses of sandwich plate structures that are too large to allow detailed meshing of the actual core geometry. Results specific to crushing of square honeycomb cores will be presented to demonstrate the effectiveness of the continuum model.

2. DYNAMIC CRUSHING UNDER CONSTANT RATE

Three-dimensional finite-element calculations have been performed to simulate the dynamic crushing response of unit cell of square honeycomb core. The unit cell of the square honeycomb core is configured as shown in Figure 1 along with the co-ordinate system used to define the orthotropic anisotropy. The height of the core unit is H, and the wall thickness of the core webs is t_c. The width of the core unit is B. The relative density of the square honeycomb core, $\bar{\rho}_c$, defined as the ratio of average density of the core to the density of material, ρ_c/ρ, (or, equivalently, as the volume of material in the core to the volume of the core) is

$$\bar{\rho}_c = 2\frac{t_c}{B} - \left(\frac{t_c}{B}\right)^2 \tag{2}$$

The junctions of the core webs with each other and with the face sheets are taken as welded, i.e. clamped. In the present paper the face sheets are assumed to be rigid.

The materials used in the numerical examples will be taken to be representative of stainless steels with relatively high strain hardening and moderate rate dependence. The true stress–strain

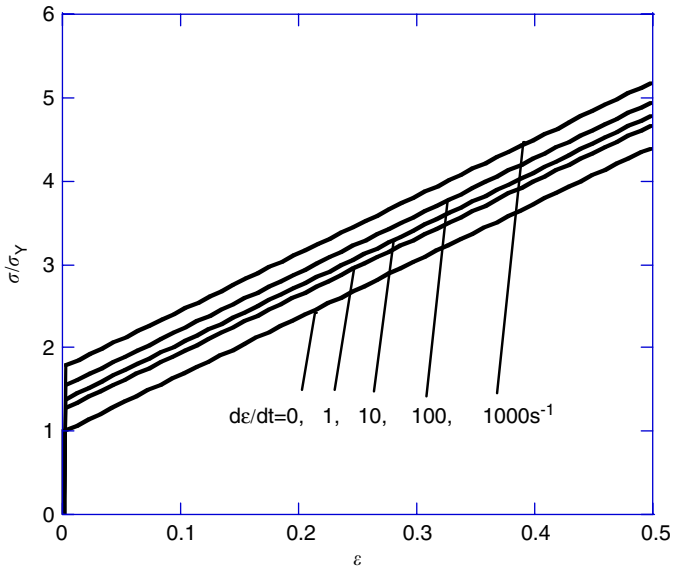

Figure 3. Stress–strain curves for various strain-rates representative of a ductile stainless steel. Computations based on these curves are presented both with and without the strain-rate dependence.

behaviour is represented by the rate-dependent bilinear relation

$$\sigma = \begin{cases} E\varepsilon, & \varepsilon \leqslant \dfrac{k\sigma_{\mathrm{Y}}}{E} \\ k\sigma_{\mathrm{Y}} + E_{\mathrm{t}}\left(\varepsilon - \dfrac{k\sigma_{\mathrm{Y}}}{E}\right), & \varepsilon > \dfrac{k\sigma_{\mathrm{Y}}}{E} \end{cases} \tag{3}$$

Here, E is Young's modulus, E_{t} is the constant tangent modulus, and σ_{Y} is the quasi-static yield stress. Rate dependence is tied to the plastic strain-rate, $\dot{\varepsilon}_{\mathrm{P}}$, through the factor elevating the flow stress: $k = 1 + (\dot{\varepsilon}_{\mathrm{P}}/\dot{\varepsilon}_0)^m$, where $\dot{\varepsilon}_0$ and m are material parameters determined by experiment. The rate-independent, quasi-static limit has $\dot{\varepsilon}_{\mathrm{P}}/\dot{\varepsilon}_0 \to 0$, or, equivalently, $k = 1$. Stress–strain curves are plotted in Figure 3 for the following choice of material parameters used in all the computations in this paper: $E = 200\,\mathrm{GPa}$, $\sigma_{\mathrm{Y}} = 350\,\mathrm{MPa}$, $E_{\mathrm{t}} = 2.4\,\mathrm{GPa}$, $\dot{\varepsilon}_0 = 4916\,\mathrm{s}^{-1}$, $m = 0.154$, $\rho = 8000\,\mathrm{kg\,m}^{-3}$, and Poisson's ratio $\nu = 0.3$. Multi-axial yield in the core webs is governed by the flow theory of plasticity based on the Mises yield surface. The geometry in all the computations has $H_{\mathrm{c}} = 0.1\,\mathrm{m}$, $B = 0.1\,\mathrm{m}$ and $t_{\mathrm{c}} \approx 2.02\,\mathrm{mm}$, corresponding to $\bar{\rho}_{\mathrm{c}} = 0.04$, representative of the relative density of sandwich plates of width 2 m with near-optimal design [1, 10].

To reveal dynamic aspects of core crushing, two compressive constant crushing-rate loadings will first be considered (Figure 2): (i) equal and opposite uniform velocities applied to the top and bottom faces, and (ii) rigidly fixed bottom face with a uniform velocity applied to the top face. The centre of mass of the core is stationary in the first loading. In the second loading, the centre of mass of the core is accelerated giving rise to different reaction stresses exerted by the core on the top and bottom faces. Of the two loadings, the second most closely

mimics a blast-loaded sandwich plate. In each case, the core webs are at rest at the start. In (i), a constant overall crushing rate is imposed by setting the top and bottom plates in motion abruptly at $t=0$ with equal and opposite constant velocities of magnitude $V_0/2$. The overall crushing strain-rate of the core, $\dot{\bar{\varepsilon}}$, and the overall (engineering) strain, $\bar{\varepsilon}$, are defined as $\dot{\bar{\varepsilon}}=V_0/H$ and $\bar{\varepsilon}=V_0 t/H$, respectively. In (ii), the same overall crushing strain-rate, $\dot{\bar{\varepsilon}}=V_0/H$, will be imposed by fixing the bottom face and setting the rigid top plate in motion abruptly with a constant downward velocity V_0. Periodic boundary conditions are imposed on the edges of the web in the cell in the 1- and 2-directions.[‡]

2.1. Geometric imperfections and their role in crush behaviour—equal and opposite applied velocities applied to the faces

The finite strain version of ABAQUS Explicit [11] has been used to carry out the dynamic computations in this paper based on the response of the unit periodic cell in Figure 1. Eight node brick elements with reduced integration are used in the calculations.[§] A representative mesh is shown in Figure 1; four elements are taken through the web thickness. The emphasis in this sub-section is on the role of imperfection amplitude and shape, the modes of deformation, and the average stress exerted by the core on the faces.

Imperfections of some form must be introduced to promote buckling of uniformly compressed plates under dynamic loading. Unperturbed, perfectly flat webs having uniform material properties will remain flat. Here, imperfections are introduced as perturbations in the geometry of the web. Since the shape of an imperfection is never known precisely, a range of imperfection shapes has been considered. It is important to include imperfection shapes with relatively short wavelengths that promote localized buckling since such modes are observed under high-velocity impact [12]. A series of possible imperfection shapes can be obtained by performing a quasi-static buckling eigenvalue analysis with ABAQUS/Standard [13] on the perfect structure. Eigenmodes generated by this analysis can be used to perturb the perfect geometry. If the same mesh is used for the eigenvalue analysis as for the dynamic analysis, the geometry shape change is readily transported from one code to the other.

Figure 4 presents the three imperfection shapes generated by the eigenvalue analysis (on the left) that will be employed in this study, along with the buckling modes they induce in the full dynamic analysis (on the right). The top part (Figure 4(a)) is imperfection-free such that dynamically deformed webs remain flat, at least until very small perturbations most likely due to meshing asymmetry or numerical round-off trigger the onset of buckling. The lower parts (Figures 4(b)–(d)) display imperfection shapes with greatly exaggerated amplitudes; the amplitudes used in the dynamic simulations are such that the maximum out-of-plane initial deflection of the web normalized by the web thickness, ζ, is $\frac{1}{5}$. The three imperfection shapes will be denoted by A, B and C, as labelled in the figure. Shape A is the lowest eigenmode. Modes B and C are not the lowest successive modes. Shape B was chosen because it has two nodal lines in the crushing direction, while Shape C has three. Shapes B and C promote

[‡]If the solution to problem (i) is strictly symmetric about the mid-plane, then it can be used to generate a solution to problem (ii) with the mid-plane stress in (i) as the stress at the bottom face in (ii), but with imposed velocity $V_0/2$ and core thickness $H/2$. Here, the solution to problem (ii) was generated using the boundary conditions stated above.

[§]Alternatively, shell elements can also be adopted in the simulations, which could save some modelling and computation time.

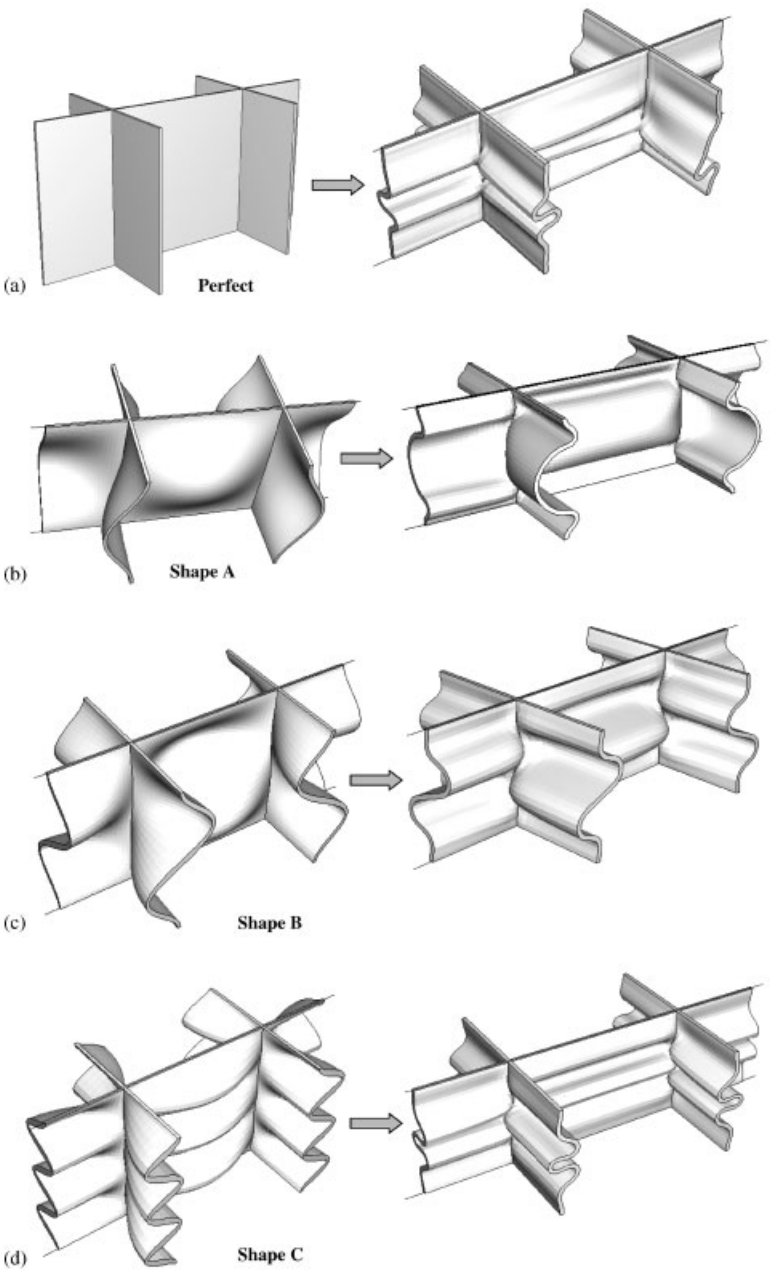

Figure 4. Deformation of square honeycomb web with various initial imperfection shapes subjected to constant equal and opposite velocities $V_0 = 50\,\mathrm{m\,s^{-1}}$ ($V_0/c_0\varepsilon_Y = 5.7$ and $\dot{\bar{\varepsilon}} = 1000\,\mathrm{s^{-1}}$) applied to the faces. Except for the perfect case, the normalized imperfection amplitude is $\zeta = \frac{1}{5}$. The imperfection shape is shown on the left and the resulting buckling mode shape at $\bar{\varepsilon} = 0.5$ is shown on the right: (a) no initial imperfection; (b) initial imperfection shape A; (c) initial imperfection shape B; and (d) initial imperfection shape C.

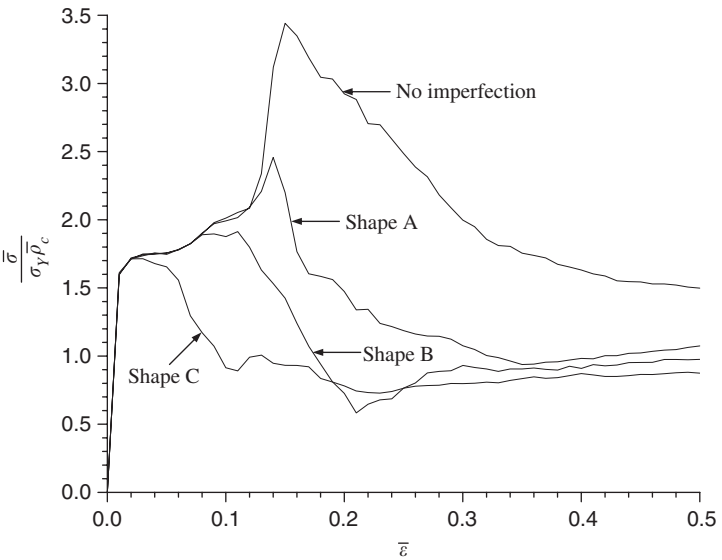

Figure 5. The influence of imperfection shape on the compressive stress exerted on the faces versus overall strain for the square honeycomb core subject to an equal and opposite constant velocity, $V_0 = 50\,\mathrm{m\,s^{-1}}$, applied to the top and bottom faces ($V_0/c_0\varepsilon_Y = 5.7$ and $\dot{\bar{\varepsilon}} = 1000\,\mathrm{s^{-1}}$). Except for the curve for the perfect case, the normalized imperfection amplitude is $\zeta = \frac{1}{5}$. Material strain-rate dependence is neglected ($k = 1$ in (3)). The core geometry is given in the text.

buckling modes with shorter crushing wavelengths. Further details of the dynamic buckling behaviour will now be discussed.

The time-dependence of the average compressive stress, $\bar{\sigma}$, exerted on the top face by the core is plotted in Figure 5 for $V_0 = \mp 50\,\mathrm{m\,s^{-1}}$ applied to the top and bottom faces, respectively, corresponding to $V_0/c_0\varepsilon_Y = 5.7$ and $\dot{\bar{\varepsilon}} = 1000\,\mathrm{s^{-1}}$. Each of the imperfect webs in Figure 5 has normalized imperfection amplitude $\zeta = \frac{1}{5}$. Even though the deformation mode that develops is not strictly symmetric (or anti-symmetric) with respect to the mid-plane of the core, the average stress on the bottom face is essentially identical to that on the top face. Material strain-rate has not been considered in these computations (by taking $k = 1$ in (3)). The average stress is normalized by $\bar{\rho}_c\sigma_Y$, which is approximately the quasi-static initial yield stress for a square honeycomb core with webs that do not buckle. The elevation of $\bar{\sigma}/\bar{\rho}_c\sigma_Y$ above unity is due both to strain hardening and to dynamic effects. The sharp up-turn in the stress for the imperfection-free core and the core with shape A occurs when the plastic wave front hits the top face after being reflected at the centre of the core by the wave travelling in the opposite direction. This sudden increase in the compressive stress promotes buckling such that the stress then falls abruptly as buckling develops with further overall straining. The core with no imperfection begins to undergo buckling at an overall strain of about 0.17, almost certainly triggered by very small numerical 'imperfections' such as round off error or meshing asymmetry.

For overall crushing strains less than about 10–15%, depending on the imperfection shape and amplitude, there is little difference between the responses of the imperfect cores and the

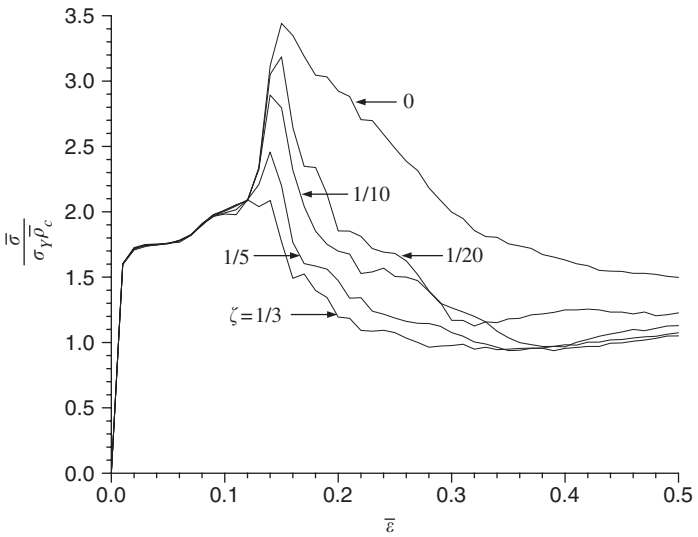

Figure 6. The effect of the normalized imperfection amplitude ζ on the compressive stress exerted on the faces versus overall strain for the square honeycomb core subject to an equal and opposite constant velocity, $V_0 = 50\,\mathrm{m\,s^{-1}}$, applied to the top and bottom faces ($V_0/c_0\varepsilon_Y = 5.7$ and $\dot{\bar{\varepsilon}} = 1000\,\mathrm{s^{-1}}$). Imperfect shape A is assumed. Material strain-rate dependence is neglected ($k = 1$ in (3)). The core geometry is given in the text.

perfect core. In this range of strain, which is deep into the plastic range and far in excess of the strain that the webs would buckle quasi-statically, the webs have been stabilized by their lateral inertia. The webs exert stresses on the faces as if they were nearly flat. As further crushing takes place, web buckles develop, and the stress exerted on the face by the imperfect cores drop below that of the perfect core. The behaviour of the core with perfect webs prior to any buckling establishes the baseline for the dynamic response at high strain-rates. Imperfection Shape C, which has the shortest wavelength of those considered, gives rise to the most rapid erosion of the stresses below those of the perfect core. At overall crushing strains of 50% the buckling shapes are fully developed (cf. Figure 4).

The effect of the imperfection amplitude ζ on the stresses exerted on the faces is shown in Figure 6 for the imperfections with shape A and $V_0/c_0\varepsilon_Y = 5.7$ ($\dot{\bar{\varepsilon}} = 1000\,\mathrm{s^{-1}}$). For overall crushing strains less than 15% the imperfection has very little effect because the webs are dynamically stabilized against buckling and resist compression as if they were flat. At larger strains, buckling deflections become significant—the larger the imperfection amplitude, the earlier buckling starts and the greater the reduction in the stresses. The behaviour displayed in Figures 5 and 6 is characteristic of problems where the loading rate is sufficiently high that axial plastic wave propagation and lateral buckling are coupled. For axial compression of columns and plates, imperfections play a more important role in dynamic buckling than in quasi-static buckling. Both amplitude and wavelength have an influence. The numerical results which follow take imperfection A with amplitude $\zeta = \frac{1}{5}$. However, as is evident in Figure 5, this is not necessarily either the most realistic imperfection or the critical imperfection. Further work on the roles of imperfections in dynamic crushing of square honeycombs is required.

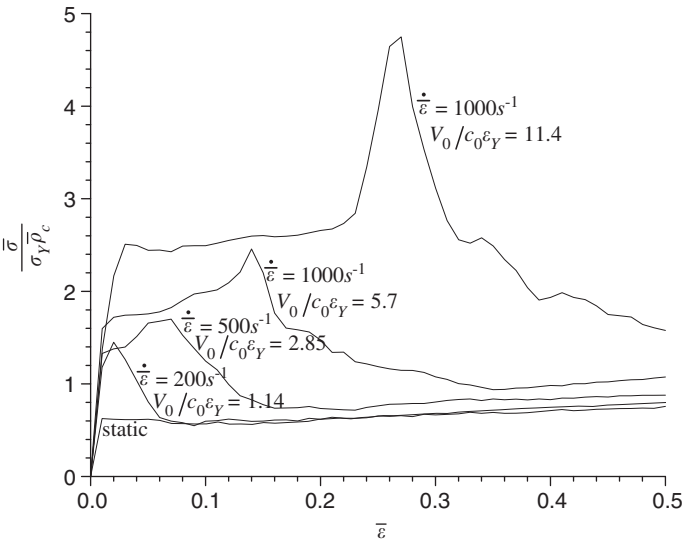

Figure 7. The effect of overall strain-rate on the compressive stress exerted on the faces versus overall strain for the square honeycomb core subject to equal and opposite constant velocities of magnitude, V_0, applied to the top and bottom faces. Imperfection shape A with normalized amplitude $\zeta = \frac{1}{5}$ is assumed. Material strain-rate dependence is neglected ($k = 1$ in (3)). The core geometry is given in the text.

Figure 7 reveals the role of the overall imposed velocity, as measured by $V_0/c_0\varepsilon_Y$, on the stress exerted on the faces for cores with a shape A imperfection and $\zeta = \frac{1}{5}$. As already mentioned, the range of imposed velocities selected in this plot is relevant to shock loaded metal sandwich panels. At each velocity, the initial response represents the behaviour of a flat web. Once buckling starts, the stress exerted on the faces falls. The delay in the onset of buckling is roughly proportional to $V_0/c_0\varepsilon_Y$. For this imperfection, buckling does not occur for strains less than about 20% if $V_0/c_0\varepsilon_Y > 10$. The delay in buckling elevates the effective core strength and enhances energy absorption.

Crushing strains in the range from 15 to 25% are representative of those expected for a square honeycomb core of a clamped sandwich plate designed to withstand large shock loads with overall deflections constrained to be no more than about one-tenth the width of the plate [10]. Thus, core crushing strains as large as 40 or 50% are generally in excess of expected levels for a well-designed sandwich plate. For crushing strains of 20% or less, the examples in Figures 5–7 suggest the following tentative conclusions: (i) the response of the unbuckled perfect core provides a relevant baseline for high-velocity crushing; (ii) the higher the velocity, the larger overall strain at which buckling sets in; and (iii) imperfection shape and amplitude are important with roles that are not entirely understood, but probably not the dominant factors determining the stresses exerted by the core on the faces at high-velocity loadings. These notions will be developed more fully in the sequel.

2.2. *Crushing behaviour—bottom face fixed, top face subject to imposed velocity*

The centre of mass of the core was stationary in the cases considered in the previous subsection. In this section, the bottom face is rigidly fixed and the top face is abruptly moved downward with velocity V_0 (Figure 2b). Average stresses on the top and bottom faces for several overall strain-rates are plotted in Figure 8, again for no material rate dependence ($k = 1$) and for imperfection shape A with amplitude $\zeta = \frac{1}{5}$. The significant difference between the stresses on the top and bottom faces is due to the asymmetry in application of the imposed velocity and the acceleration of the centre of mass of the core. At a given overall strain-rate, the inertial contribution to the stress acting on the top face is larger than the corresponding stress for previous case due to the fact that $V_0/c_0\varepsilon_Y$ is twice as large. A small initial jump in the stress acting on the bottom face occurs when the elastic wave hits that face. The stress on the bottom face then remains nearly at the compressive yield stress until the plastic wave front hits that face, at which point the compressive stress increases abruptly to about twice the stress experienced by the top face, as would be expected for a wave reflected at a rigid support when the tangent modulus is constant. It is readily verified that the strain at which this occurs is given by $\bar{\varepsilon} \cong V_0/c_P$, where c_P is the plastic wave speed (1).

Prior to the point where the plastic wave reaches the bottom face the stress exerted on the top face is unaffected by the thickness H of the core. If the webs are flat and do not buckle, one-dimensional elastic–plastic wave theory can be used to obtain an analytical estimate of the stress exerted on the top face associated with abruptly moving it at velocity V_0 [3, 7, 8]. Based

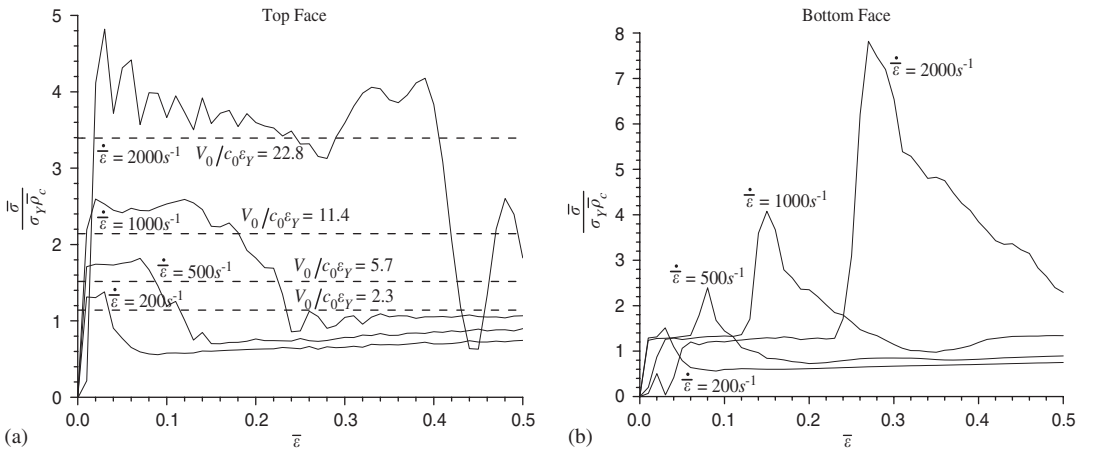

Figure 8. Compressive stresses exerted on the top (a) and bottom (b) faces by the core as a function of strain for square honeycomb core held rigidly on the bottom face and subject to a constant velocity, V_0, on the top face for several overall strain-rates. Imperfect shape A is assumed with normalized amplitude $\zeta = \frac{1}{5}$. Material strain-rate dependence is neglected ($k = 1$ in (3)). The dashed lines in (a) are the predictions from (4) applicable to a perfect core prior to buckling and prior to arrival of the reflected plastic wave from the bottom face. The core geometry is given in the text.

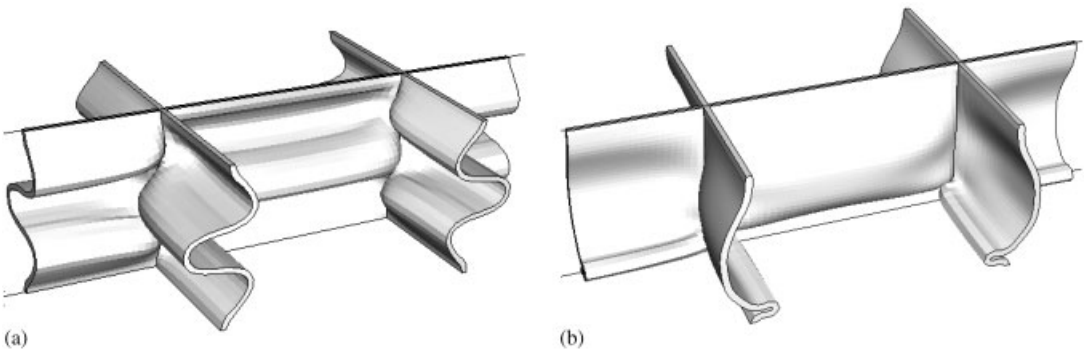

Figure 9. Buckled configurations at $\bar{\varepsilon} = 0.5$ for cores held rigidly on the bottom face and subject to a constant velocity on the top face: (a) quasi-static loading with $\dot{\bar{\varepsilon}} \approx 0\,\mathrm{s}^{-1}$; and (b) $\dot{\bar{\varepsilon}} = 2000\,\mathrm{s}^{-1}$.

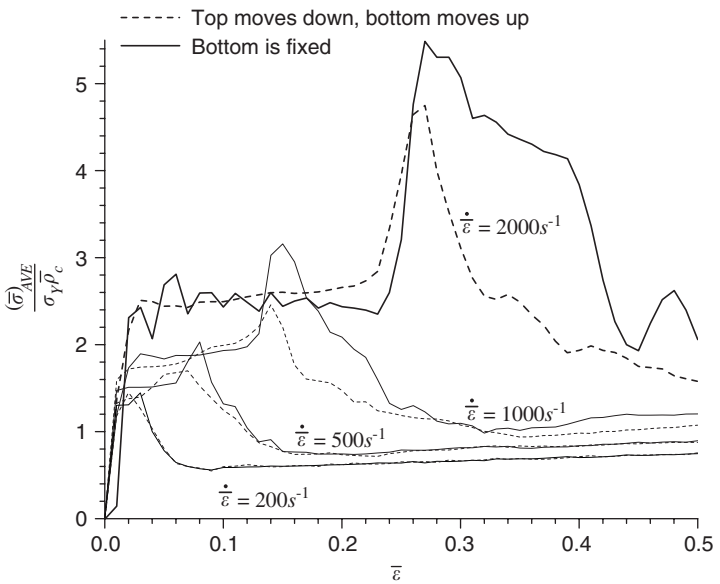

Figure 10. Comparison of the average of the stresses acting on the top and bottom faces when the bottom face is fixed and the top face is subject to an imposed velocity (from Figure 7) with the stress on the top (or bottom) face for a core subject to equal and opposite velocity of its faces (from Figure 6). Imperfection shape A is assumed with normalized amplitude $\zeta = \frac{1}{5}$.

on small strain theory for the rate-independent limit of the bilinear material (3), the result is

$$\frac{\bar{\sigma}}{\bar{\rho}_c \sigma_Y} \cong 1 + \sqrt{\frac{E_t}{E}} \left(\frac{V_0}{c_0 \varepsilon_Y} - 1 \right) \tag{4}$$

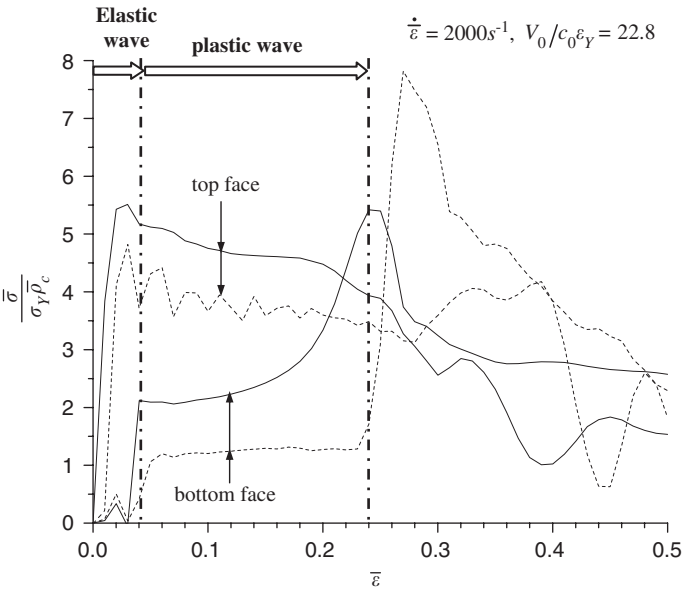

Figure 11. The influence of material strain-rate on the stresses exerted on the top and bottom faces for the case when the bottom face is fixed and the top face is subject to an imposed velocity with $V_0/c_0\varepsilon_Y = 22.8$. Results with (solid curves) and without (dashed curves) material rate dependence are shown. Imperfection shape A is assumed with normalized amplitude $\zeta = \frac{1}{5}$.

where $V_0/(c_0\varepsilon_Y) > 1$ for the stress to exceed yield. This estimate is plotted in Figure 8(a), revealing that it indeed provides a good approximation to the reaction stress until the plastic wave returns from the bottom plate.

At high impact velocities, buckling does not have a pronounced effect on the stress exerted on the faces before the plastic wave hits the bottom face. The large jump in compressive stress then promotes buckling near the bottom plate. Shortly thereafter, buckling gives rise to the rapid drop in the stress acting on the bottom face. The drop in stress on the top face occurs when the plastic wave returns from the bottom plate. Pictorial evidence for this scenario is seen in Figure 9, where the buckled deflections at $\bar{\varepsilon} = 0.5$ are shown for both quasi-static loading and the high-velocity case with $V_0/(c_0\varepsilon_Y) = 22.8$ and $\dot{\bar{\varepsilon}} = 2000\,\mathrm{s}^{-1}$. While the buckling deflection varies smoothly through the core under quasi-static loading, it tends to be localized near the bottom face under high-velocity loading.

An unusual correlation between behaviours for the loading case considered in this section with that in the last section is evident in Figure 10. In Figure 10, the average of the compressive stresses exerted on the top and bottom faces in Figure 8 is compared with the stress exerted on the top (or bottom) face from Figure 7. To a surprising degree of accuracy, the two sets of results are nearly the same. We are unaware of any general principle underlying this correlation, but it can be shown that the two sets of results are exactly equal for the solutions to the two corresponding problems for the linear one-dimensional wave equation.

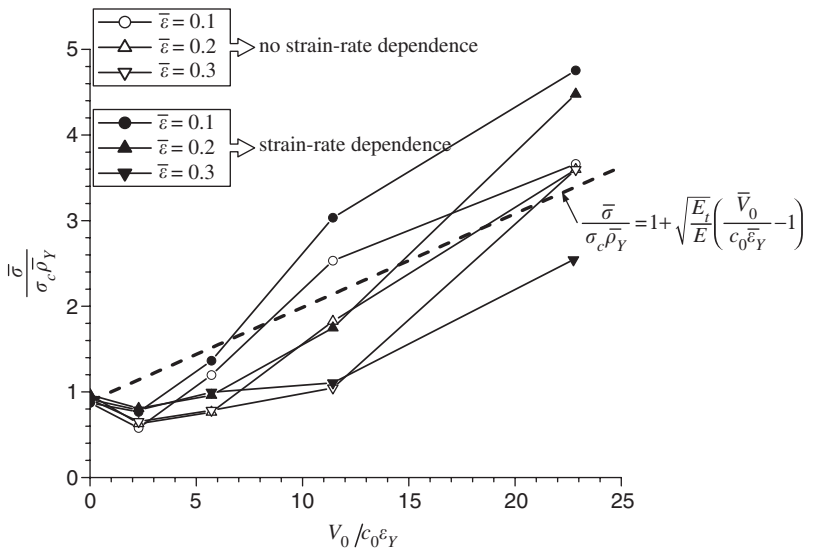

Figure 12. Compressive stress exerted on the top face by square honeycomb core at several overall crushing strains as a function of $V_0/(c_0\varepsilon_Y)$ for cores held rigidly on the bottom face and subject to velocity V_0 on the top face. Imperfection shape A is assumed with normalized amplitude $\zeta = \frac{1}{5}$. The dashed line is the prediction from (4) applicable to a perfect core of rate-independent material prior to buckling and prior to arrival of the reflected plastic wave from the bottom face.

2.3. Material rate dependence—bottom face fixed, top face subject to imposed velocity

The role of material rate dependence on the stresses exerted on the top and bottom faces is brought out in Figure 11 where results with and without rate dependence are displayed for a core subject to $V_0/(c_0\varepsilon_Y) = 22.8$ ($\dot{\bar{\varepsilon}} = 2000\,\mathrm{s}^{-1}$) with a shape A imperfection and $\zeta = \frac{1}{5}$. Before the plastic wave hits the bottom face, the elevation of the front face stress due to material rate dependence relative to that without rate dependence is in accord with what one would expect from the elevation in the flow stress (cf. Figure 3) for a strain-rate $\dot{\bar{\varepsilon}} = 2000\,\mathrm{s}^{-1}$. When the plastic wave hits the bottom face, the material rate dependence smoothes out the jump in the stress and tends to make the stress drop less precipitous when buckling dominates the behaviour.

A cross-plot of the normalized stress acting on the top face as a function of the dimensionless parameter, $V_0/(c_0\varepsilon_Y)$, at three overall strain levels is presented in Figure 12. Results have been computed with and without material rate dependence. The dynamic strengthening of the core displayed in Figure 12 is similar to that found for coupled plastic wave propagation and dynamic column buckling [3] over the same range of $V_0/(c_0\varepsilon_Y)$. The trends are approximately captured by (4) based on the small strain, rate-independent limit. During the period while the plastic wave is progressing through the core, $V_0/(c_0\varepsilon_Y)$ is the most important dimensionless group governing the dynamic response. As emphasized earlier, the range of $V_0/(c_0\varepsilon_Y)$ plotted in Figure 12 is relevant to blast-loaded metal sandwich plates.

3. A CONTINUUM MODEL OF THE CORE

For large structures built up from sandwich plates, it may not be feasible or even sensible to mesh the complete three-dimensional details of the core in a finite-element analysis. Instead, one would employ a continuum description of the core that smears out its geometric details but approximately reproduces its effective stress–strain behaviour under the deformation histories of interest. Buckling deformations of the core, whether under crush or shear, generally extend from one face to the other, and, therefore, they can only be represented in an approximate way by a continuum model that embeds the effect of buckling as if it were a local phenomenon. In other words, the separation of scales usually invoked to justify the formal averaging process leading to a continuum representation of a medium does not hold for the core. The continuum representation of the core is inherently approximate in this sense.

In this section, a continuum model is laid out describing the elastic–plastic response of orthotropic sandwich core materials under multi-axial stressing. The model accounts for hardening or softening behaviour that can differ for stressing in each of the six fundamental stressing histories in orthotropic axes. Mass is distributed uniformly throughout the thickness of the core in the model such that overall inertial resistance is replicated. Material rate dependence is included and the effect of the strain-rate on strengthening the core via the mechanism of core web stabilization against buckling is also modelled.

Let the x_i-axes be aligned with the orthotropic core axes. Introduce overall, or average, stress, strain and plastic strain vectors in the usual way with

$$\begin{aligned}\boldsymbol{\sigma} &= (\sigma_1, \sigma_2, \sigma_3, \sigma_4, \sigma_5, \sigma_6) \equiv (\sigma_{11}, \sigma_{22}, \sigma_{33}, \sigma_{13}, \sigma_{23}, \sigma_{12})\\ \boldsymbol{\varepsilon} &= (\varepsilon_1, \varepsilon_2, \varepsilon_3, \varepsilon_4, \varepsilon_5, \varepsilon_6) \equiv (\varepsilon_{11}, \varepsilon_{22}, \varepsilon_{33}, 2\varepsilon_{13}, 2\varepsilon_{23}, 2\varepsilon_{12})\\ \boldsymbol{\varepsilon}^{\mathrm{P}} &= (\varepsilon_1^{\mathrm{P}}, \varepsilon_2^{\mathrm{P}}, \varepsilon_3^{\mathrm{P}}, \varepsilon_4^{\mathrm{P}}, \varepsilon_5^{\mathrm{P}}, \varepsilon_6^{\mathrm{P}},) \equiv (\varepsilon_{11}^{\mathrm{P}}, \varepsilon_{22}^{\mathrm{P}}, \varepsilon_{33}^{\mathrm{P}}, 2\varepsilon_{13}^{\mathrm{P}}, 2\varepsilon_{23}^{\mathrm{P}}, 2\varepsilon_{12}^{\mathrm{P}})\end{aligned} \tag{5}$$

Let the 6×6 symmetric matrices of overall elastic moduli and compliances representing the elastic response of the core in the unbuckled state be such that

$$\begin{aligned}\boldsymbol{\sigma} &= \mathbf{L}\boldsymbol{\varepsilon}\\ \boldsymbol{\varepsilon} &= \mathbf{M}\boldsymbol{\sigma}\end{aligned} \tag{6}$$

The basic inputs to the model prescribed below are the six rate-dependent stress–strain curves that characterize the plastic response of the continuum core under conditions when each of the above six (*positive*) *stress components acts singly*. Specifically, when σ_i is the only non-zero stress component, let $\hat{\sigma}_i(\varepsilon_i^{\mathrm{P}}, \dot{\varepsilon}_i^{\mathrm{P}})$ denote the hardening (or softening) function specifying the dependence of σ_i on the associated plastic strain component, $\varepsilon_i^{\mathrm{P}}$, when the plastic strain-rate, $\dot{\varepsilon}_i^{\mathrm{P}}$, is positive and constant. Thus, for example, $\hat{\sigma}_1(\varepsilon_1^{\mathrm{P}}, \dot{\varepsilon}_1^{\mathrm{P}})$ is the stress–plastic strain response when the continuum core is deformed under uniaxial tension in the 1-direction at constant strain-rate $\dot{\varepsilon}_1^{\mathrm{P}}$. Note that, by definition, the input functions, $\hat{\sigma}_i(\varepsilon_i^{\mathrm{P}}, \dot{\varepsilon}_i^{\mathrm{P}})$, are positive. When compression is relevant in a particular application, as in the case of core crush, input data for compression can be substituted in place of tension data for any of the three uniaxial stress component, as will be obvious later. The two versions of the multi-axial constitutive model, independent hardening and coupled hardening, are formulated such that they reproduce the input stress–strain data when each of the six stress components acts singly.

Specific forms for the input functions $\hat{\sigma}_i(\varepsilon_i^{\mathrm{P}}, \dot{\varepsilon}_i^{\mathrm{P}})$ are now suggested for the square honeycomb core with emphasis on crushing, illustrating the process for other cores as well. The objective is to come up with a simple description of each of the input functions that captures the most important features of the non-linear core behaviour associated with plastic buckling, necking or even fracture. It is important to distinguish between the constitutive response of the continuum core, as measured for example by $\hat{\sigma}_3(\varepsilon_3^{\mathrm{P}}, \dot{\varepsilon}_3^{\mathrm{P}})$ for core crushing, and the relation such as those plotted in Section 2 between the stress exerted on the sandwich faces and the overall strain. The stress on the faces involves plastic wave propagation, acceleration of core mass and other influences in addition to the purely constitutive response. Section 4.1 addresses the identification of $\hat{\sigma}_3(\varepsilon_3^{\mathrm{P}}, \dot{\varepsilon}_3^{\mathrm{P}})$ such that it reproduces (approximately) the stresses exerted on the faces for selected loading cases when a continuum simulation is made with the constitutive model.

Denote the tensile true stress–strain behaviour of the material comprising the core webs under constant plastic strain-rate by $\sigma(\varepsilon^{\mathrm{P}}, \dot{\varepsilon}^{\mathrm{P}})$. Take the 3-direction perpendicular to the face sheets as in Figure 1. For tension (compression) in the 3-direction prior to buckling or necking of the webs, $\hat{\sigma}_3(\varepsilon_3^{\mathrm{P}}, \dot{\varepsilon}_3^{\mathrm{P}}) = (2/\sqrt{3})\bar{\rho}_{\mathrm{c}}\sigma(\varepsilon^{\mathrm{P}}, \dot{\varepsilon}^{\mathrm{P}})$, where the factor $(2/\sqrt{3})$ (for web materials having a Mises yield surface) reflects the constraint of the faces such that the webs undergo plane strain tension (compression). In the 1-direction, prior to buckling or necking, $\hat{\sigma}_1(\varepsilon_1^{\mathrm{P}}, \dot{\varepsilon}_1^{\mathrm{P}}) = (\bar{\rho}_{\mathrm{c}}/2)\sigma(\varepsilon_1^{\mathrm{P}}, \dot{\varepsilon}_1^{\mathrm{P}})$, with a similar expression for the 2-direction. With $\tau(\gamma^{\mathrm{P}}, \dot{\gamma}^{\mathrm{P}})$ as the stress–strain behaviour of the base material in shear, the out-of-plane shear stress–strain behaviour of the core in the $(1, 3)$ axes prior to buckling can be approximated by $\hat{\sigma}_4(\varepsilon_4^{\mathrm{P}}, \dot{\varepsilon}_4^{\mathrm{P}}) = (\bar{\rho}_{\mathrm{c}}/2)\tau(\varepsilon_4^{\mathrm{P}}, \dot{\varepsilon}_4^{\mathrm{P}})$, with a similar expression for $\hat{\sigma}_5$ in the $(2, 3)$ axes. In-plane shear behaviour in the $(1, 2)$ axes is of little consequence as long as $\hat{\sigma}_6$ is taken to be small because the core is very weak in this mode.

We illustrate how buckling can be modelled in making a choice for the input function $\hat{\sigma}_3$ which incorporates the strong rate dependence of the onset of plastic buckling noted in the numerical examples. In what follows, it is assumed that yielding precedes buckling, as will usually be the case except for cores with unusually low density. Were that not the case, another choice for the form of $\hat{\sigma}_3$ might be necessary. Assume the compressive branch of the stress–strain behaviour is used (taking $\hat{\sigma}_3$ and $\varepsilon_3^{\mathrm{P}}$ as positive in compression for this purpose) and consider the prescription pictured in Figure 13. A form for $\hat{\sigma}_3$ with features similar to those in Figure 13 has been proposed and implemented in Reference [14] for cores with truss members in an alternative approach to core modelling based on homogenization methods. Specifically, $\hat{\sigma}_3$ is taken to be

$$\hat{\sigma}_3 = \begin{cases} k\bar{\sigma}_{\mathrm{Y}} + E'_{\mathrm{t}}\varepsilon_3^{\mathrm{P}}, & 0 \leqslant \varepsilon_3^{\mathrm{P}} \leqslant \widehat{\varepsilon}_3^{\mathrm{P}} \\ (k\bar{\sigma}_{\mathrm{Y}} + E'_{\mathrm{t}}\,\widehat{\varepsilon}_3^{\mathrm{P}}) - 2E'_{\mathrm{t}}(\varepsilon_3^{\mathrm{P}} - \widehat{\varepsilon}_3^{\mathrm{P}}), & \widehat{\varepsilon}_3^{\mathrm{P}} < \varepsilon_3^{\mathrm{P}} \leqslant (0.25k\bar{\sigma}_{\mathrm{Y}}/E'_{\mathrm{t}} + 1.5\,\widehat{\varepsilon}_3^{\mathrm{P}}) \\ 0.5k\bar{\sigma}_{\mathrm{Y}}, & (0.25k\bar{\sigma}_{\mathrm{Y}}/E'_{\mathrm{t}} + 1.5\,\widehat{\varepsilon}_3^{\mathrm{P}}) < \varepsilon_3^{\mathrm{P}} \leqslant 1 \\ 0.5k\bar{\sigma}_{\mathrm{Y}} + 2E'_{\mathrm{t}}(\varepsilon_3^{\mathrm{P}} - 1), & 1 < \varepsilon_3^{\mathrm{P}} \end{cases} \tag{7}$$

expressed in true stress and logarithmic strain. Here, the factor k incorporates the material strain-rate dependence included in (3), $\bar{\sigma}_{\mathrm{Y}}$ is the overall quasi-static yield stress defined as $\bar{\sigma}_{\mathrm{Y}} = (2/\sqrt{3})\bar{\rho}_{\mathrm{c}}\sigma_{\mathrm{Y}}$, and the overall Young's modulus is $E' = (2/\sqrt{3})\bar{\rho}_{\mathrm{c}}E$. The core response is elastic with $\sigma_3 = E'\varepsilon_3$ for $\varepsilon_3 \leqslant k\bar{\sigma}_{\mathrm{Y}}/E$, while $\varepsilon_3^{\mathrm{P}} = \varepsilon_3 - \sigma_3/E'$ for $\varepsilon_3 \geqslant k\bar{\sigma}_{\mathrm{Y}}/E$. The

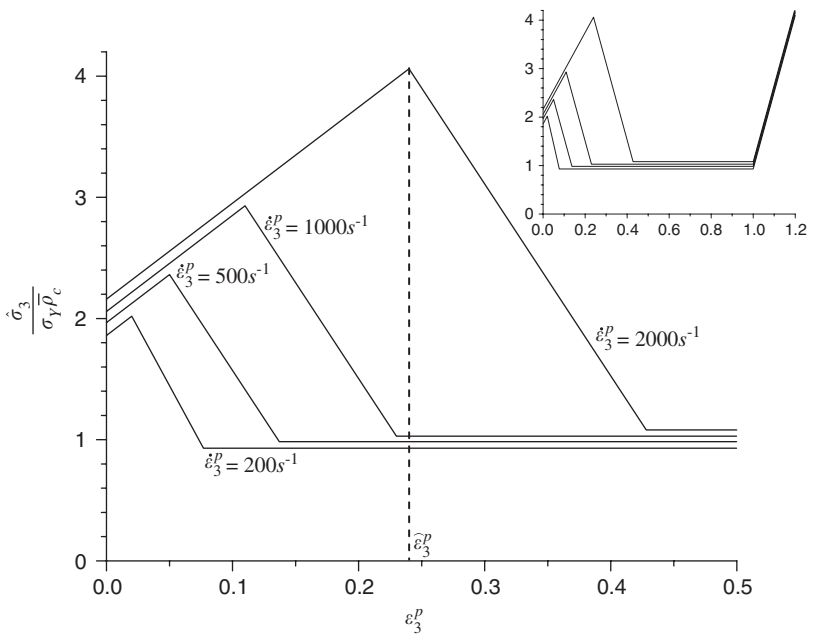

Figure 13. Form of the input function assumed for crushing of square honeycomb core. The full specification is given by (7).

overall tangent modulus, E'_t, is given in terms of the material tangent modulus in (3) by $E'_t = (2/\sqrt{3})\bar{\rho}_c E E_t/(E - E_t)$. The plasic strain parameter associated with the onset of buckling in the constitutive model is denoted by $\widehat{\varepsilon}_3^P$; it is primarily a function of the strain-rate $\dot{\varepsilon}_3^P$ but it also depends on the *material rate dependence and details of the core geometry*. It must be identified by calibration either with experimental data or with selected numerical simulations (Section 4.1). The slope, $2E'_t$, governing softening and compaction hardening in (7) was chosen after several trial and error iterations such as those described in Section 4.1, as was the stress, $0.5k\bar{\sigma}_Y$, and strain range of the flat minimum. These parameters had much less influence on dynamic crushing predictions from the continuum model than $\widehat{\varepsilon}_3^P$.

An ellipsoidal yield surface is invoked that generalizes Hill's surface for orthotropic plastically incompressible materials. Ellipticity of the surface is allowed to change to account for differential hardening or softening. Associated plastic flow is also invoked such that plastic strain-rates are normal to the yield surface. Due to their highly open, porous structure, many core structures undergo relatively little transverse plastic strain when they are stressed uniaxially in any of the three directions of orthotropy. The plastic strain-rate ratios (analogous to Poisson ratios in the elastic range) are then well approximated as being zero. The relations given below are special cases of the more general constitutive law proposed in Reference [15] where transverse strains are not zero.

When the transverse plastic strains under uniaxial stressing parallel to the axes of orthotropy are zero, the ellipsoidal yield surface for orthotropic compressible materials can be written in

the form

$$f \equiv \sigma_{\text{eff}} - \sigma_0 = 0 \tag{8}$$

where the effective stress σ_{eff} is defined by

$$\left(\frac{\sigma_{\text{eff}}}{\sigma_0}\right)^2 = \left(\frac{\sigma_{11}}{\hat{\sigma}_{11}}\right)^2 + \left(\frac{\sigma_{22}}{\hat{\sigma}_{22}}\right)^2 + \left(\frac{\sigma_{33}}{\hat{\sigma}_{33}}\right)^2 + \left(\frac{\sigma_{12}}{\hat{\sigma}_{12}}\right)^2 + \left(\frac{\sigma_{13}}{\hat{\sigma}_{13}}\right)^2 + \left(\frac{\sigma_{23}}{\hat{\sigma}_{23}}\right)^2$$

$$= \sum_i \left(\frac{\sigma_i}{\hat{\sigma}_i}\right)^2 \tag{9}$$

The stress quantity σ_0 is a *fixed* reference stress that can be chosen arbitrarily (e.g. $\sigma_0 = 1$ MPa); it is simply a scaling factor. Normality is assumed such that $\dot{\varepsilon}_i^{\text{P}} = \dot{\lambda}\partial f/\partial\sigma_i$. The effective plastic strain-rate, $\dot{\varepsilon}_{\text{eff}}^{\text{P}}$, defined such that the plastic work is given by $\sigma_{ij}\dot{\varepsilon}_{ij}^{\text{P}} = \sigma_{\text{eff}}\dot{\varepsilon}_{\text{eff}}^{\text{P}}$, turns out to be

$$\dot{\varepsilon}_{\text{eff}}^{\text{P2}} = \sum_i \left(\frac{\hat{\sigma}_i}{\sigma_0}\dot{\varepsilon}_i^{\text{P}}\right)^2 \tag{10}$$

The plastic strain-rate components are given by

$$\dot{\varepsilon}_i^{\text{P}} = \frac{\sigma_0^2\sigma_i}{\sigma_{\text{eff}}\hat{\sigma}_i^2}\dot{\varepsilon}_{\text{eff}}^{\text{P}} \tag{11}$$

There are well-known limitations to ellipsoidal yield surfaces. Some cellular materials (e.g. truss lattice materials [16]) have yield surfaces that are more polyhedral-like than ellipsoidal. Under combined crushing and out-of-plane shear, conventional hexagonal honeycomb has a yield surface with nearly a linear interaction between the compressive stress and shear stress [5] when the honeycomb is buckled. The present ellipsoidal surface would overestimate the honeycomb strength under combinations of these two stress components. On the other hand, for plastic deformation prior to buckling of the square honeycomb web, the ellipsoid surface correctly reproduces the behaviour expected for combinations of crush and out-of-plane shear parallel to the axes of orthotropy assuming that the Mises yield surface controls local yield in the webs. The same is true for combinations of in-plane stretch and out-of-plane shear parallel to the axes of orthotropy. When buckling occurs, these assertions can no longer be made. The advantage of the present model is the flexibility it affords in reproducing the six fundamental stress histories. For some materials under certain combinations of stress, the ellipsoidal yield surface represents a compromise of accuracy whose consequences must be judged within the context of the application.

Two hardening laws for multi-axial stressing are proposed: *independent hardening* and *coupled hardening*. Both reproduce the six input stress–strain curves, $\hat{\sigma}_i(\varepsilon_i^{\text{P}}, \dot{\varepsilon}_i^{\text{P}})$, precisely when σ_i acts singly such that $\dot{\varepsilon}_i^{\text{P}}$ is positive and constant.

Independent hardening: This is the simplest recipe. Under multi-axial stressing, assume that each of the six hardening functions, $\hat{\sigma}_i$, is affected only by the associated plastic strain component, ε_i^{P}, and its rate. Let $\dot{\eta}_i^{\text{P}} = |\dot{\varepsilon}_i^{\text{P}}|$ and take each of the hardening functions as $\hat{\sigma}_i(\eta_i^{\text{P}}, \dot{\eta}_i^{\text{P}})$. For stressing with $\sigma_i > 0$ as the only component, this reduces to the input function when $\dot{\varepsilon}_i^{\text{P}}$

is constant. This hardening law is akin to that used in conjunction with yield surfaces that are polyhedral in shape with no interaction between the individual stress components in either the yield condition or the hardening relation. The code DYNA has a constitutive module of this class that has been used to model sandwich cores. It employs a 'rectangular' polyhedral yield surface in orthotropic axes comprised of planes specified by constant values of each of the stress components, and it invokes independent hardening. This constitutive model has been systematically studied in Reference [17]. The present ellipsoidal surface with independent hardening lies within the rectangular surface coinciding only at the intercepts with the stress axes.

Coupled hardening: As before, assume the six independent hardening laws, $\hat{\sigma}_i(\varepsilon_i^{\mathrm{P}}, \dot{\varepsilon}_i^{\mathrm{P}})$, as input. Under multi-axial stressing, this recipe ties the changes of each of these hardening functions to straining in each component through the effective plastic strain-rate in a manner that is analogous to what is known as Taylor hardening in single crystal theory. Specifically, take the ith hardening function to be $\hat{\sigma}_i(\eta_i^{\mathrm{P}}, \dot{\eta}_i^{\mathrm{P}})$, where

$$\dot{\eta}_i^{\mathrm{P}} = (\sigma_0/\hat{\sigma}_i)\dot{\varepsilon}_{\mathrm{eff}}^{\mathrm{P}} \tag{12}$$

Note that this recipe reduces to $\dot{\eta}_i^{\mathrm{P}} = \dot{\varepsilon}_i^{\mathrm{P}}$ when $\sigma_i > 0$ is the only non-zero stress component. Thus, this prescription has each of the six hardening functions depending on $\varepsilon_{\mathrm{eff}}^{\mathrm{P}}$ in such a way that the model replicates the input stress–strain data when any of the six stress components acts singly and the associated plastic strain-rate is constant. For the special case when the six hardening functions change in direct proportion to one another (called uniform hardening), coupled hardening reduces to the hardening assumption made in conventional isotropic hardening. For uniform hardening with no rate dependence, only one input stress–strain curve is required to specify the hardening behaviour under multiaxial stressing and the model reduces to that proposed in Reference [18].

The two versions of the model are fully specified. It only remains to obtain the incremental relations among the stresses, strains and plastic strains. Plastic straining at *constant strain-rates* requires $\dot{f} = \dot{\sigma}_{\mathrm{eff}} = 0$, or

$$\sum_i \left(\frac{\sigma_i \dot{\sigma}_i}{\hat{\sigma}_i^2} - \frac{\sigma_i^2}{\hat{\sigma}_i^3} \frac{\partial \hat{\sigma}_i}{\partial \eta_i^{\mathrm{P}}} \dot{\eta}_i^{\mathrm{P}} \right) = 0 \tag{13}$$

Here, $\dot{\eta}_i^{\mathrm{P}} = \varepsilon_i^{\mathrm{P}} \dot{\varepsilon}_i^{\mathrm{P}} / \eta_i^{\mathrm{P}}$ (no summation) for independent hardening, and $\dot{\eta}_i^{\mathrm{P}}$ is given by (12) for coupled hardening. The stress increments satisfy

$$\dot{\sigma}_i = \sum_j L_{ij}(\dot{\varepsilon}_j - \dot{\varepsilon}_j^{\mathrm{P}}) \tag{14}$$

Changes in the elastic moduli due to deformation of the core are not taken into account. Using (13), it is readily shown that

$$\dot{\varepsilon}_{\mathrm{eff}}^{\mathrm{P}} = \left[\Lambda + \frac{\sigma_0^2}{\sigma_{\mathrm{eff}}} \sum_i \sum_j L_{ij} \frac{\sigma_i \sigma_j}{\hat{\sigma}_i^2 \hat{\sigma}_j^2} \right]^{-1} \sum_i \sum_j L_{ij} \frac{\sigma_i}{\hat{\sigma}_i^2} \dot{\varepsilon}_j \tag{15}$$

where for independent hardening

$$\Lambda = \frac{\sigma_0^2}{\sigma_{\text{eff}}} \sum_i \frac{|\sigma_i|^3}{\hat{\sigma}_i^5} \frac{\partial \hat{\sigma}_i}{\partial \eta_i^{\text{P}}} \tag{16}$$

while for coupled hardening

$$\Lambda = \sigma_0 \sum_i \frac{\sigma_i^2}{\hat{\sigma}_i^4} \frac{\partial \hat{\sigma}_i}{\partial \eta_i^{\text{P}}} \tag{17}$$

Equations (11), (14) and (15) provide the tangent moduli relating the stress and strain increments: $\dot{\boldsymbol{\sigma}} = \bar{\mathbf{L}}\dot{\boldsymbol{\varepsilon}}$. If $\bar{\mathbf{L}}$ is non-singular, $\dot{\boldsymbol{\varepsilon}} = \bar{\mathbf{M}}\dot{\boldsymbol{\sigma}}$ where $\bar{\mathbf{M}} = \bar{\mathbf{L}}^{-1}$. The plastic strain-rate, $\dot{\boldsymbol{\varepsilon}}^{\text{P}}$, was assumed constant in deriving the above constitutive equations. As is customary in generalizing constant strain-rate data to plasticity applications were the strain-rate itself varies, the accelerations of the plastic strains are ignored in the equations, if for no other reason that the stress–strain data under varying strain-rates is generally not available. Thus, the above equations are proposed as the core constitutive model under general conditions of stressing and straining.

4. CALIBRATION OF THE CONTINUUM MODEL AND COMPARISON WITH THREE-DIMENSIONAL SIMULATIONS FOR UNIAXIAL CRUSHING

The focus in this section will be on dynamic crushing deformations. The three-dimensional simulations in Section 2, wherein the faces are subject to equal and opposite velocities are used to calibrate a candidate input function $\hat{\sigma}_3(\varepsilon_3^{\text{P}}, \dot{\varepsilon}_3^{\text{P}})$. Initial imperfection shape A with normalized amplitude $\zeta = \frac{1}{5}$ is assumed for core in all three-dimensional calculations involved in this section. Then, to see how successfully the continuum model can simulate other cases, predictions based on this input function will be compared with three-dimensional simulations for (i) the case when the bottom face is fixed and (ii) the case of free flight of the sandwich where the top face is subject to an initial velocity with the core and bottom face unconstrained and initially at rest.

4.1. A candidate input function, $\hat{\sigma}_3$, and its calibration

As described in Section 3, for compression of the square honeycomb in the 3-direction prior to buckling, we have $\hat{\sigma}_3(\varepsilon_3^{\text{P}}, \dot{\varepsilon}_3^{\text{P}}) = (2/\sqrt{3})\bar{\rho}_{\text{c}}\sigma(\varepsilon^{\text{P}}, \dot{\varepsilon}^{\text{P}})$, neglecting the small influence of imperfections prior to buckling, where $\sigma(\varepsilon^{\text{P}}, \dot{\varepsilon}^{\text{P}})$ is the stress–strain behaviour of the base material. In the approach adopted here, the remaining parameters characterizing $\hat{\sigma}_3$ in Figure 13, and most importantly, $\widehat{\varepsilon}_3^{\text{P}}$, are chosen to give a good fit to the three-dimensional results such as those in Figure 7 for the case where the faces are subject to equal and opposite uniform velocities. The process of identifying the parameters characterizing $\hat{\sigma}_3$ is necessarily an iterative one. Various schemes are possible. The following approach was used here.

For a given set of the parameters, a simulation is carried out using the continuum model for a specific overall compressive strain-rate, $\dot{\bar{\varepsilon}}$. In each such simulation, $\widehat{\varepsilon}_3^{\text{P}}$ is taken to be independent of $\dot{\varepsilon}_3^{\text{P}}$ and fixed at the value chosen for $\dot{\bar{\varepsilon}}$. The calibration problem for crushing of the continuum core can be simplified as a plane strain problem. Four-node bilinear elements with reduced

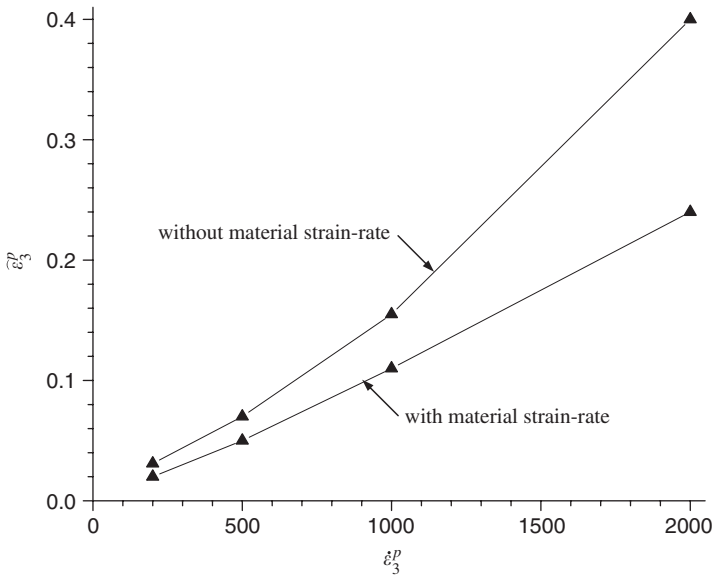

Figure 14. Dependence of $\widehat{\varepsilon}_3^{\mathrm{P}}$ on strain-rate and on whether material rate dependence is taken into account. This parameter controls the onset of plastic buckling in the continuum model.

integration and hourglass control are used in the calculations. Eight elements are taken through the thickness of the core. Additional studies showed that more elements did not significantly change the overall response, except that it did produce more high-frequency oscillatory 'noise' of the type seen in Figure 8. The computations are carried out using ABAQUS Explicit. The overall stress–strain response so computed for the continuum representation of the core is then compared with the corresponding unit cell prediction for the same crushing deforming from the full three-dimensional simulation. This process is repeated with a different choice of continuum model parameters, based largely on trial and error, until satisfactory agreement between the two simulations is obtained for various $\dot{\bar{\varepsilon}}$ over the range of interest. The most important parameter, $\widehat{\varepsilon}_3^{\mathrm{P}}$, in the continuum representation depends strongly on the overall strain-rate and somewhat less strongly on material rate sensitivity (Figure 14).

Figure 14 emphasizes the large effect played by the strain-rate in delaying the onset of plastic buckling. Because it elevates the compressive stress, material rate dependence decreases the parameter $\widehat{\varepsilon}_3^{\mathrm{P}}$ controlling the onset of buckling in the continuum model. As mentioned earlier, neither the slope of the softening response nor the final slope governing compaction has nearly as large an influence as $\widehat{\varepsilon}_3^{\mathrm{P}}$. The overall responses from the continuum simulations described above based on the final choice of parameters are compared with the three-dimensional crushing results in Figure 15 for $\dot{\bar{\varepsilon}} = 200$ and $2000\,\mathrm{s}^{-1}$, both with and without material strain-rate dependence. The essential features of the dynamic response of the three-dimensional core are reproduced by the continuum model. Moreover, the quantitative agreement between the two sets of simulations is also reasonably good, especially considering that the core response involves coupled plastic wave propagation and plastic buckling. The elevations in stress exerted by the core on the faces due to the delay in buckling and material rate dependence are both

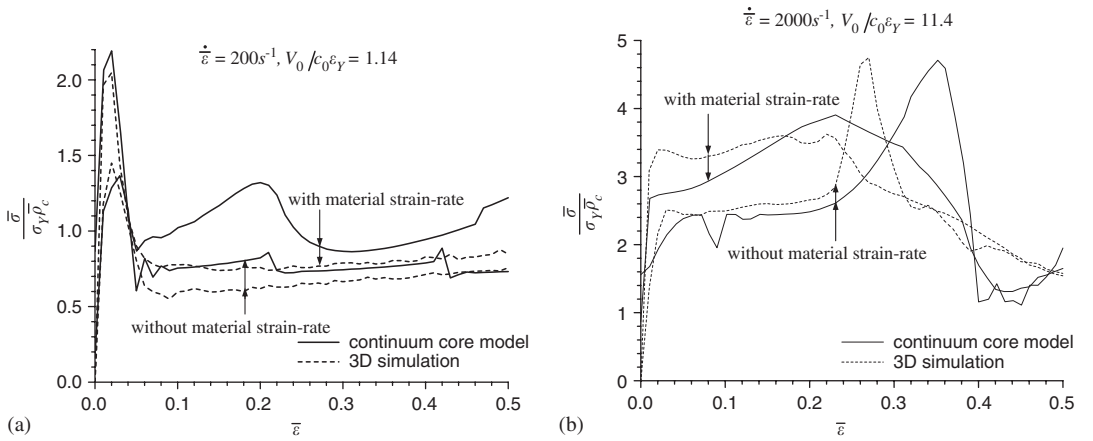

Figure 15. Comparison of simulations based on the continuum core model with those based on full three-dimensional meshing of the core at two overall strain-rates: (a) $\dot{\bar{\varepsilon}} = 200\,\mathrm{s}^{-1}$; and (b) $\dot{\bar{\varepsilon}} = 2000\,\mathrm{s}^{-1}$. Equal and opposite velocities are applied to the top and bottom faces.

captured, as is the dramatic rise in stress just prior to buckling when the plastic wave reflected from the core mid-plane reaches the face.

4.2. Comparisons for the case where the bottom face is fixed

In the calibration step, for simplicity in evaluating the constitutive response, the strain-rate at every point in the core is taken to be the overall rate, $\dot{\bar{\varepsilon}}$. In applications of the continuum constitutive model, the local strain-rate at each point in the core, $\dot{\varepsilon}_3^{\mathrm{P}}$, is used in evaluating $\hat{\sigma}_3(\varepsilon_3^{\mathrm{P}}, \dot{\varepsilon}_3^{\mathrm{P}})$. Thus, in the calculations carried out in this sub-section and the next, the point-wise rate dependence of $\widehat{\varepsilon}_3^{\mathrm{P}}$ on $\dot{\varepsilon}_3^{\mathrm{P}}$ in Figure 14 is taken into account.

With the parameters of $\hat{\sigma}_3$ specified according to the calibration carried out above, simulations are made using the continuum model for the case where the top face is subject to uniform velocity V_0 and the bottom face is fixed. This case brings in the effect of acceleration of the centre of mass of the core resulting in a stress difference between the top and bottom faces. The two sets of predictions for the stresses, computed with and without material strain-rate dependence, are compared in Figure 16 for $V_0/c_0\varepsilon_{\mathrm{Y}} = 22.8$ ($\dot{\bar{\varepsilon}} = 2000\,\mathrm{s}^{-1}$). The continuum model approximately captures the three contributions to dynamic strengthening of the core at high strain-rates that have been highlighted earlier in the paper. In particular, it can be seen that the significant difference between the stresses exerted on the top and bottom faces is correctly replicated. Coupling of plastic wave propagation and buckling is also captured through the input function $\hat{\sigma}_3$. Thus, even though the input function has been calibrated at fixed values of strain-rate, it successfully reproduces responses in applications where the strain-rate varies through the thickness of the core. The largest error occurs after buckling occurs when the stresses drop. Given the sensitivity of the buckling pattern in the core webs to the overall strain-rate, it is not surprising that this aspect is not with high fidelity by the continuum model.

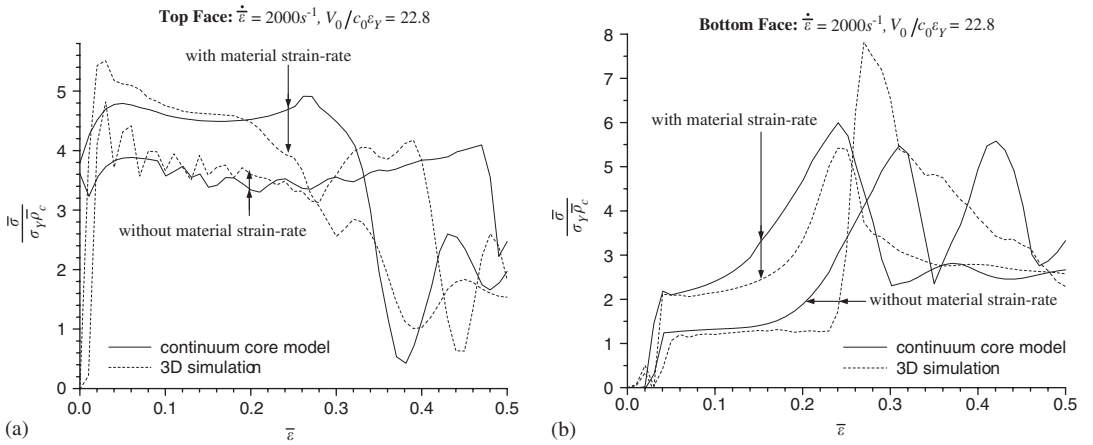

Figure 16. Comparison of simulations based on the continuum core model with those based on full three-dimensional meshing of the core at an overall strain-rate $\dot{\bar{\varepsilon}} = 2000\,\mathrm{s}^{-1}$. The bottom face is fixed and the top face is moved at constant velocity. Compressive stresses exerted on the top face and bottom face are shown.

4.3. Comparisons for free flight

The following case illustrates application of the continuum model to a problem where the overall strain-rate is initially high and then decreases with time. Consider free flight of a sandwich plate initially at rest where motion is initiated by abruptly imposing an initial velocity $V_0 = 200\,\mathrm{m\,s}^{-1}$ on the top face. The top face flies into the core, compressing it such that it, in turn, exerts stress on the back face. After a period of non-uniform motion and crushing, the entire assembly moves with common velocity. In the example considered here, each of the faces is assigned the same mass/area as the core. Other details of the core are the same as those used in the examples throughout the paper, and the parameters characterizing $\hat{\sigma}_3$ are those determined in Section 4.1. Conservation of momentum gives the final common velocity as $V_0/3$, and two-thirds of the initial kinetic energy imparted to the top face is dissipated in core crushing in this example.

A comparison of simulations based on the continuum model and those from three-dimensional simulations that fully mesh the core webs is given in Figure 17 in the form of curves of overall crushing strain, $\bar{\varepsilon}$, as a function of time. The curves are terminated when the assembly has achieved the maximum crushing strain and the common velocity. A slight oscillation of the overall strain continues beyond this point due to elastic vibrations of the system as it undergoes free flight. Material rate dependence reduces the crushing strain. The free flight case is relevant to intense shock loadings, and it is evident that the continuum model is successful in simulating core crushing.

5. CONCLUSIONS

Three effects enhancing the effective strength of honeycomb metal sandwich cores under dynamic crushing have been highlighted in this paper: material rate dependence, inertial

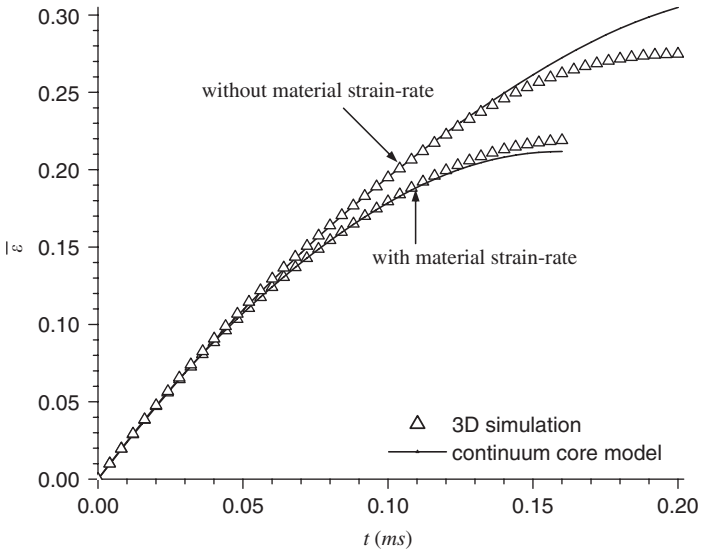

Figure 17. Comparison between simulations of the evolution of the overall crushing strain based on the continuum core model and those based on three-dimensional meshing of the core for crushing under free flight conditions where the sandwich plate is unconstrained. The core and bottom face are initially at rest and the top face is set in motion abruptly with velocity $V_0 = 200\,\mathrm{m\,s^{-1}}$. Details of the sandwich plate are given in the text.

resistance and inertial buckling stabilization. Of the three, buckling stabilization is the most significant and the most difficult to characterize and model. Buckling stabilization is important in the range of relative velocities of the faces produced by shock loadings; it becomes significant when the relative crushing velocity of the faces satisfies $V_0/c_0\varepsilon_Y > 5$, where c_0 and ε_Y are the elastic wave speed and yield strain of the base material. For loadings at these rates, axial plastic wave propagation and plastic buckling occur over comparable time scales and substantial plastic straining takes place prior to buckling. The critical role of initial imperfections in triggering buckling requires further investigation.

A continuum constitutive model of the core has been proposed that incorporates the three strengthening effects in crushing and which is capable of representing the core under multi-axial stressing, including combinations of crush, shear and stretch. The purpose of the constitutive relation is to replace detailed meshing of core members in sandwich structures in large finite-element models, thereby reducing the size of the numerical computation. A decision to invoke a continuum model of the core necessarily involves a tradeoff between loss of fidelity associated with the continuum model and the difficulty and computational cost of full core meshing.

It has been emphasized that a continuum representation of the core is inherently approximate in the sense that under most circumstances buckling does not occur on a scale smaller than the core thickness. On the other hand, the continuum representation is able to approximately capture most of the complexities of dynamic crushing behaviour, including plastic wave propagation through the core prior to buckling, delayed buckling and the erosion of strength as buckling develops. A critical step in application of the continuum model is identification of the input functions, $\hat{\sigma}_i(\varepsilon_i^{\mathrm{P}}, \dot{\varepsilon}_i^{\mathrm{P}})$, that specify the constitutive model. The process requires a functional form

for $\hat{\sigma}_i(\varepsilon_i^{\mathrm{P}}, \dot{\varepsilon}_i^{\mathrm{P}})$ be assumed; then the parameters specifying the form must be determined by fitting predictions to either experimental data or to computations based on fully meshed core geometries. An approach for the input function for crushing using results based on unit cells with fully meshed cores has been illustrated here for a specific core. The parameters of the input function must be determined for each core in terms of its specific set of geometric and material parameters. Identification procedures are also addressed in Reference [14]. Further work to develop the identification of the input functions is needed both for the square honeycomb subject to the other stress components and for other core geometries [15].

Finally, we note that the rate-dependent constitutive model proposed in this paper has been implemented as a VUMAT subroutine in the finite-element code ABAQUS Explicit.

ACKNOWLEDGEMENTS

This work has been supported in part by the ONR under Grants N00014-02-1-0700 and GG10376-114934 and in part by the Division of Engineering and Applied Sciences, Harvard University. The authors are indebted to helpful suggestions from N. A. Fleck and T. Belytschko.

REFERENCES

1. Xue Z, Hutchinson JW. A comparative study of impulse-resistant metallic sandwich plates. *International Journal of Impact Engineering* 2004; **30**:1283–1305.
2. Fleck NA, Deshpande VS. The resistance of clamped sandwich beams to shock loading. *Journal of Applied Mechanics* 2004; **71**:386–401.
3. Vaughn D, Canning M, Hutchinson JW. Coupled plastic wave propagation and column buckling. *Journal of Applied Mechanics* 2005; **72**:1–8.
4. Gibson LJ, Ashby MF. *Cellular Solids*: *Structure and Properties* (2nd edn). Cambridge University Press: Cambridge, MA, 1997.
5. Mohr D, Doyoyo M. Large plastic deformation of metallic honeycomb: orthotropic rate-independent constitutive model. *International Journal of Solids and Structures* 2004; **41**:4435–4456.
6. Cote F, Deshpande VS, Fleck NA, Evans AG. The out-of-plane compressive behavior of metallic honeycombs. *Materials Science and Engineering A* 2004; **380**:272–280.
7. Taylor GI. *The Scientific Papers of G.I. Taylor*, vol. 1. Cambridge University Press: London, 1958.
8. von Karman T, Duwez P. The propagation of plastic deformation in solids. *Journal of Applied Physics* 1950; **21**:987–994.
9. Calladine CR, English RW. Strain-rate and inertia effects in the collapse of two types of energy-absorbing structure. *International Journal of Mechanical Sciences* 1984; **26**:689–701.
10. Hutchinson JW, Xue Z. Metal sandwich plates optimized for pressure impulses. *International Journal of Mechanical Sciences* 2005; **47**:545–569.
11. *ABAQUS/Explicit User's Manual*, *Version 6.0.* Karlsson and Sorensen Inc.: Hibbit, 2001.
12. Abrahamson GR, Goodier JN. Dynamic flexural buckling of rods within an axial plastic compression wave. *Journal of Applied Mechanics* 1966; **33**:241–247.
13. *ABAQUS/Standard User's Manual*, *Version 6.0.* Karlsson and Sorensen Inc.: Hibbit, 2001.
14. Rabczuk T, Kim JY, Samaniego E, Belytschko T. Homogenization of sandwich structures. *International Journal for Numerical Methods in Engineering* 2004; **61**:1009–1027.
15. Xue Z, Varziri A, Hutchinson JW. Non-uniform hardening constitutive model for compressible orthotropic materials with applications to sandwich plate cores. *Computer Modeling in Engineering and Sciences*, in press.
16. Deshpande VS, Fleck NA, Ashby MF. Effective properties of the octet-truss lattice material. *Journal of the Mechanics and Physics of Solids* 2001; **49**:1747–1769.
17. Hanssen AG, Langseth M, Hopperstad OS. Crush behavior of foam-based components: validation of numerical simulations. *Advanced Engineering Materials* 2002; **4**:771–776.
18. Xue Z, Hutchinson JW. Constitutive model for quasi-static deformation of metallic sandwich cores. *International Journal for Numerical Methods in Engineering* 2004; **61**:2205–2238.

